Pergamon

Int. J. Solids Structures Vol. 33, No. 10, pp. 1453–1477, 1996
Elsevier Science Ltd
Printed in Great Britain

0020–7683(95)00101–8

PREDICTION OF FORCE–TIME HISTORIES IN THICK STEEL PLATES DUE TO PENETRATION BY TUNGSTEN RODS AT VELOCITIES OF 1.5–2.5 km s^{-1}

J. E. SALIBA, S. DHAR, D. J. GROVE and N. S. BRAR
University of Dayton Research Institute, 300 College Park, Dayton, OH 45469, U.S.A.

(*Received* 26 *September* 1994; *in revised form* 10 *April* 1995)

Abstract—An analytical model has been proposed to predict the force–time history in an isotropic plate due to penetration by a projectile. The analytical model developed considers the prediction of shape and size of the cavity, pressure distribution along the cavity wall and force–time history for the penetration event. The shape and the radius of the cavity obtained from the model are compared with the experiment and with the finite element simulation. Six penetration experiments were performed in 4340 steel plates by long tungsten rods ($L/D = 11$) at velocities in the range of 1.5–2.5 km s^{-1}. These experiments were then simulated using the EPIC91 Research Code. From the experiments, cavity radius, terminal velocity and reduction in rod length are compared with the finite element simulations. The simulated cavity radius, cavity depth, cavity expansion velocity and force–time histories are comparable with those obtained from the cavity growth and expansion model. Initially, an idealized analytical force–time history was compared with the simulation. The results showed that the force–time history is characteristic of the penetration event. Finally, we evaluated the influence of target thickness and striking velocity of the projectile on the analytical force–time history.

NOTATION

a, a_f, $\bar{a}$	local cavity radius as a function of cavity depth, final (maximum) cavity radius and dimensionless cavity radius, respectively
$\dot{a}$, $\ddot{a}$	local cavity's radial expansion velocity and acceleration as a function of cavity depth and time
b, $\bar{b}$	location of elastic–plastic interface and dimensionless elastic–plastic interface, respectively
$\dot{b}$, $\ddot{b}$	dimensionless elastic–plastic interface velocity and acceleration, respectively
c, C_R	sound velocity and Raleigh wave speed
E, Y	modulus of elasticity and dynamic yield strength of the target material
F	force exerted by projectile on the target
k, $\bar{k}$	location of elastic wave front and dimensionless elastic wave front, respectively
$\dot{k}$, $\ddot{k}$	dimensionless elastic, stress-free interface velocity and acceleration, respectively
N	strain hardening value
P, $\bar{P}$	total time varying pressure and dimensionless time varying pressure.
P_S, P_D	static and dynamic pressure, respectively
K^*	numerical parameter [see eqn (1)]
$\bar{o}$	dimensionless stress-free region
r, r_0	Eulerian radial coordinate and initial radial particle position, respectively
S_1, S_2	normalized radial and hoop stresses, respectively
S_1^P, S_1^e	plastic and elastic integration constants, respectively
$\bar{S}_{1(S)}$, $\bar{S}_{1(D)}$	dimensionless static and dynamic stresses, respectively
u_r, v_r	particle displacement and velocity in the radial direction, respectively.
z, z_f	local cavity depth (Eulerian coordinates) and final (maximum) cavity depth, respectively
$\dot{z}_{int}$, Z^*	projectile–target interface velocity and numerical parameter [see eqn (1)], respectively
α	calibration parameter (dimensionless time) [see eqn (2)]
α_e, α_p	dimensionless densities [see eqn (29)]
$\bar{\beta}$	function of density and yield strength [see eqn (3)]
γ	dimensionless radial displacement
δ', β'	material constants given by eqn (54)
η, $\bar{\eta}$	limit of integration, normalized limit of integration, respectively
η_e, η_p	initial locations of elastic and plastic shock fronts, respectively
$\dot{\eta}_e$, $\dot{\eta}_p$	dimensionless velocities of wave fronts in the elastic and plastic regions, respectively.
ξ, ξ_0	normalized radial coordinate, initial location of the particle

ρ_0, ρ_t	density of the target at time $t = 0$ and at time $t > 0$, respectively
ρ_{ip}, ρ_{le}	locked densities in the plastic and elastic regions, respectively
$\zeta_{\bar{\xi}}$	normalized particle velocity in the radial direction
$\zeta_{\bar{\delta}}^{P}$, $\zeta_{\bar{\delta}}^{e}$	dimensionless particle velocities in the plastic and elastic regions, respectively
$\zeta_{\bar{\delta}}^{e}$, $\zeta_{\bar{\delta}}^{0}$	dimensionless particle velocities in the elastic and stress-free regions, respectively
σ_r, σ_θ, σ_z	radial, circumferential and axial stresses, respectively
ν_t	Poisson's ratio of the target material
$\bar{\sigma}$, $\bar{\varepsilon}$	effective stress and strain, respectively
ε_r, ε_θ, ε_z	radial, circumferential and axial strain, respectively
ε_l, ε_{le}, ε_{lp}	locking strain, locked elastic strain and locked plastic strain, respectively
τ_n, γ_n	octahedral shear stress and strain, respectively
ΔM_z	change in axial momentum
Δt	time step

1. INTRODUCTION

The accurate modeling of the local events of the global structural response of a thick semi-infinite target due to penetration by a long rod projectile must include the formation of a cavity in the target with varying shape (hemisphere, ogive, cone etc.) and size (radius), local damage (bulging) of the target in the front and rear surface of the cavity, and the decrease in projectile length with increase in the nose diameter. The size of the cavity depends on whether the target is considered as a compressible or incompressible material. The penetration of the target was explained based on spherical or cylindrical cavity expansion theory, achieved over 30 years ago by Bishop *et al.* (1945) for the quasi-static punch indentation process. In their work, they obtained the solutions for the static expansion of cylindrical and spherical cavities in an infinite medium. The extension to penetration problems under hypervelocity impact was obtained by Goodier using results from the dynamic spherical cavity expansion studies reported by Hopkins.

The idealized instantaneous force exerted on the local cavity at any time step during the penetration would be the product of the total pressure exerted on the local cavity and its surface area. The total pressure consists of static and dynamic terms.

The objective is to determine the global structural response of the target due to penetration by a projectile, and to develop a model capable of (i) describing the local events, such as the shape and radial expansion attributes of the local cavity during penetration, and (ii) determining the instantaneous force exerted on the local cavity at any time step during the penetration.

This paper addresses: (a) the penetration experiments in 4340 steel plates by long tungsten rods ($L/D = 11$) at velocities in the range of 1.5–2.5 km s^{-1}, (b) the finite element simulation of the penetration experiment using the EPIC91 code, (c) a mathematical expression to describe the shape and radial expansion attributes of the local cavity during penetration, and (d) a comparison of idealized and simulated force–time history during penetration. The derivation of the analytical model in predicting the pressure distribution along the cavity wall and the force–time history for the penetration event is given in Section 4. Finally, the research concludes with the evaluation of the influence of target thickness and striking velocity of the projectile on the characteristic force–time history.

2. EXPERIMENTAL ANALYSIS

2.1. *Description of projectile and targets*

The tungsten projectiles, 5 mm in diameter and 55 mm long ($L/D = 11$ and mass = 18.8 g), were prepared from as-received tungsten alloy rods. The tungsten alloy (WN307F, swaged and aged) had a density of 17.67 g cm^{-3} (99.6% of the theoretical density) and a Rockwell hardness (R_c) of 44.6. The 4340 steel target plates, with a 304.8 mm nominal diameter, were sliced from a 304.8 mm cold-rolled round stock with thickness ranging from 25.4 to 100 mm. Both surfaces of the plates were turned to make them flat and parallel. The plates were subsequently heat treated to an R_c hardness of about 30.

Table 1. Comparison of experimental and simulation results for rod exit data

Shot number	Simulated impact velocity (km s^{-1})	Pre-impact rod inclination (°)		Exit velocity of rod (km s^{-1})		Dimensionless exit length of rod (final/initial)	
		Exp.	Sim.	Exp.	Sim.	Exp.	Sim.
4-1529	2.00	0.75	0.0	1.31	1.49	0.111	0.178
4-1566	1.60	16.5	0.0	—	—	—	—
4-1567	2.00	6.3	0.0	1.64	1.74	0.273	0.356
4-1568	2.66	4.2	0.0	2.25	2.42	0.157	0.280
4-1569	2.00	10.8	0.0	—	1.89	0.606	0.662
4-1570	2.00	8.0	0.0	—	—	—	—

Table 2. Comparison of experimental and simulation results for cavity diameters

Shot number	Entry (mm)		Middle (mm)		Exit (mm)	
	Exp.	Sim.	Exp.	Sim.	Exp.	Sim.
4-1529	10.0	13.0	9.75	9.5	11.75	14.0
4-1566	6.0	11.5	—	8.0	—	—
4-1567	11.5	13.5	10.5	9.5	12.0	14.0
4-1568	15.0	15.5	13.5	11.0	16.0	19.0
4-1569	11.0	13.5	10.0	10.0	11.5	15.5
4-1570	12.0	12.5	10.0	7.5	—	—

Table 3. Baseline grid for target plates

Shot number	Thickness (mm)	Radius (mm)	Number of nodes	Number of elements
4-1529	63.5	152.4	3788	7400
4-1566	63.5	152.4	3788	7400
4-1567	50.8	152.4	3038	5920
4-1568	63.5	152.4	3788	7400
4-1569	25.4	152.4	1538	2960
4-1570	101.6	152.4	6038	11840

2.2. *Two-stage gas gun launch and results*

Projectiles were launched using the 50/20 mm two-stage gas gun at the University of Dayton Research Institute, to velocities up to about 2.7 km s^{-1}. Projectile velocities were measured to within 0.5% accuracy using time-of-flight measurements between four laser-photo detector stations located along the range center line. Pre-impact yaw and pitch of the projectile were measured with an orthogonal set of flash X-rays triggered by a delayed pulse from the laser beam. Penetrator exit velocity and residual length were monitored by a second set of orthogonal flash X-rays mounted behind the target plate.

Table 1 summarizes the data on impact velocity, pre-impact penetrator inclination, residual velocity and length of the penetrator from the six experiments. Table 2 summarizes the measured cavity diameter in the target plates at entry, middle and exit locations.

3. FINITE ELEMENT SIMULATION

Finite element simulation of long rod penetration in semi-infinite steel target has been investigated by many authors using CTH. A summary of their work is given in Anderson and Walker (1991). We have used the 1991 version of the EPIC Research Code (EPIC91R) (Johnson and Stryk, 1991) to simulate all six penetration experiments. A baseline 2-D axisymmetric finite element grid was created for each experimental configuration and is summarized in Table 3. All elements were generated in a crossed triangle arrangement. Elements on the rod–plate interface were eroded (eliminated) when their equivalent plastic

strain exceeded an erosion strain criterion of 1.5. In all the simulations, the target plates were modeled without restraints. Figures 1 and 2 shows the initial and final baseline grid plots from the calibrated simulations.

3.1. *Calibration with experiments*

Shot 4-1529 was chosen for the initial calibration of the finite element simulations, since it was the "best" shot in terms of pre-impact rod inclination (pitch and yaw). The calibration objectives were to match the following experimental data: (a) the length of the exiting projectiles, (b) the velocity of the exiting projectile, (c) the dimensions of the cavity in the target plate. The first simulation of shot 4-1529 employed the Johnson–Cook strength and fracture models to describe the material behavior in both the tungsten rod and the steel plate. Reasonable agreement with shot 4-1529 was finally obtained by preventing damage growth (DAM = 0) and thermal softening ($M = 0$) in modeling the material behavior of the tungsten rod. Maintaining the above material behavior restrictions, the remaining five shots were simulated. Table 1 shows a comparison of the experimental and simulated results for rod exit data, and Table 2 shows a comparison of the experimental and simulated results for cavity diameters.

The exit velocity of the projectile obtained from the finite element simulation is 6–14% greater than the experiments. The residual length of the projectile obtained from the finite element simulation is 5–12% greater than observed in the experiments. The cavity diameter in the middle section of the target obtained from the finite element simulation is 2.5–25% lower than the experiment. The variations in exit velocity, residual length of the projectile and the cavity diameter are due to impact inclination of the projectile. The small angle of inclination gives comparable results between experiment and the finite element analysis.

3.2. *Analytical expression defining the cavity shape*

The projectile is assumed to be a flat-ended cylinder (rod) which impacts a homogeneous, isotropic target plate at normal incidence. Immediately upon impact, the projectile begins to penetrate the target. As the penetration proceeds, the projectile's nose remains in constant contact with the target and a cavity forms inside the target. This contact zone defines the target's local cavity. The target's local cavity is defined as that part of the global cavity in which radial expansion is occurring, i.e. in the immediate vicinity of the nose of the penetrating rod. The geometry of local cavity shape is shown in Fig. 3. In this figure, the horizontal axis indicates radial distance from the axis of symmetry and the vertical axis represents local cavity depth. There are an infinite number of local cavities formed during the penetration process. The cavity shape function given by eqn (1) has been formulated to describe the characteristic shape of these local cavities:

$$a(z) = \begin{cases} a_f\left[1 - K^*\left(1 - \dfrac{z}{z_f}\right)^2\right]^\alpha, & Z^* < z \leqslant z_f \\ \left(\dfrac{C_R}{\dot{z}_{int}}\right) z & 0 \leqslant z \leqslant Z^*, \end{cases} \tag{1}$$

where the local cavity radius $a(z)$ varies between 0 (at the base of the cavity) and a_f, the characteristic final (maximum) cavity radius. Also, z is the local cavity depth, z_f is the characteristic final (maximum) cavity depth, C_R is the Raleigh wave speed, $\dot{z}_{int}$ is the projectile–target interface velocity (assumed constant for complete penetration) and α is the calibration parameter, or mathematically it represents dimensionless time. In eqn (2), the two expressions and their first derivatives (with respect to z) must be equal to each other at Z^*, i.e. the cavity shape function is smooth and continuous. For an arbitrary α ($0 < \alpha \leqslant 1$), this condition can be satisfied by uniquely determining the parameters K^* and Z^* through an iterative numerical scheme. Assuming that $\dot{z} = \dot{z}_{int}$ at higher velocities, the partial derivative of the shape function $a(z)$ with respect to time, $\dot{a}(z, t)$, provides the following expression for the local cavity's radial expansion velocity:

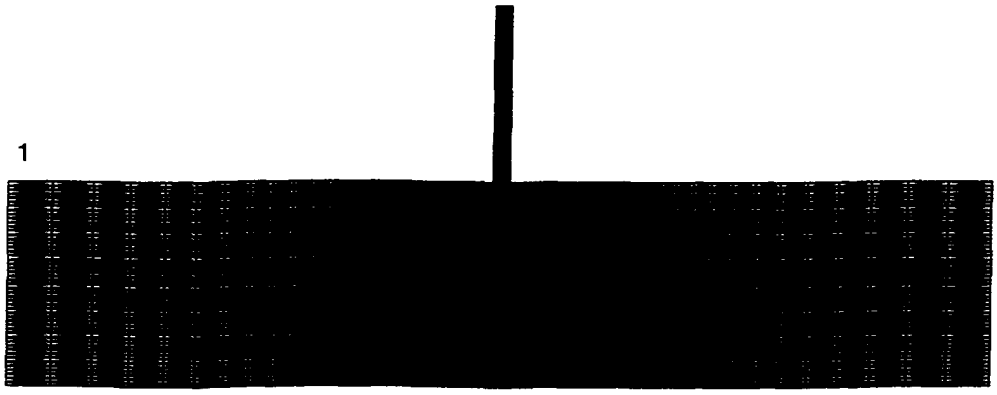

Fig. 1. Initial baseline grid plot.

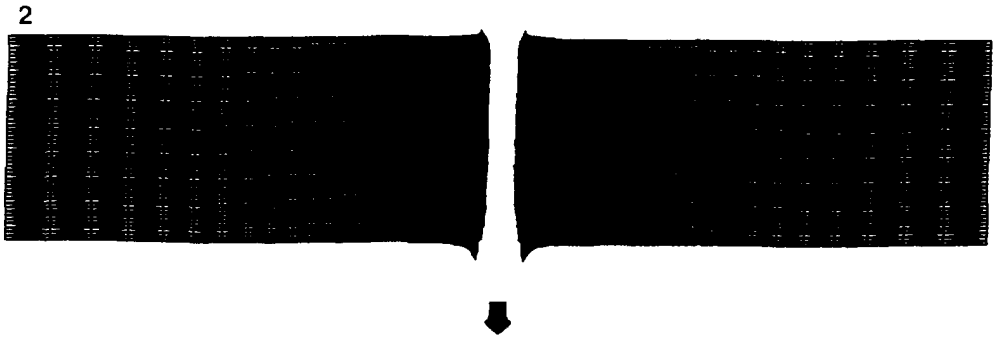

Fig. 2. Final baseline grid plot.

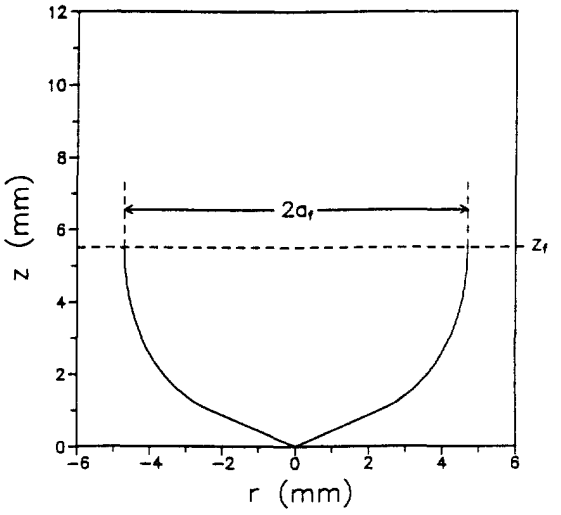

Fig. 3. Geometry of local cavity shape.

$$\dot{a}(z,t) = \begin{cases} \left(\dfrac{2\alpha a_f K^*}{z_f}\right)\left(1-\dfrac{z}{z_f}\right)\left[1-K^*\left(1-\dfrac{z}{z_f}\right)^2\right]^{\alpha-1}\dot{z}_{int}, & Z^* < z \leqslant z_f \\ C_R, \quad 0 \leqslant z \leqslant Z^*. \end{cases} \tag{2}$$

Figure 4 illustrates the cavity shape function for various values of $\dot{z}_{int}$ and α. Increasing the interface velocity from 0.1 to 2.5 mm μs^{-1} for a given value α changes the shape of the cavity from cylinder to ogive. This shape function can also be used to model the nose of the rigid projectile. The nose geometry can be spherical, ogival, conical and cylindrical.

3.3. *Cavity attributes from simulation*

The EPIC91R code was modified accordingly to produce additional output pertaining to the rod–plate interface velocity and the local cavity's shape and radial expansion characteristics. Cavity growth in the axial direction was examined through a time history plot of the simulated axial rod–plate interface position, shown in Fig. 5. This curve, essentially a straight line, suggests a relatively constant rod–plate interface velocity (≈ 1.2 km s^{-1}) during the penetration process. A constant interface velocity assumption may be reasonable for complete penetration. In the case of partial penetration, however, the rod–plate interface velocity is fairly constant during the penetration event, but eventually this velocity must decrease to zero.

Output data from the EPIC simulation of shot 4-1529 were used to analyse the characteristics of local cavity expansion and growth in the target plate. The simulated local cavity shape data from 20 equally spaced axial locations throughout the thickness of the target plate were used to calibrate the parameters in the local cavity shape defined by eqn (1). The data and the cavity shape functions are superimposed in Fig. 6. The cavity shape function parameters are $a_f = 4.7$ mm, $z_f = 5.5$ mm, $\dot{z}_{int} = 1.15$ mm μs^{-1}, $\alpha = 0.35$, $K^* \approx 1.245$, $C_R = 2.94$ mm μs^{-1} and $Z^* \approx 0.86365$ mm. Local cavity expansion occurs in the radial direction and cavity growth occurs in the axial direction. The characteristics of the cavity's radial expansion were determined by examining the simulated time histories of cavity radii for 20 equally spaced axial locations throughout the target thickness. The data from these profiles, superimposed in Fig. 7, exhibit a distinctive pattern. Initially, upon arrival of the penetrating rod, the radial expansion rate is highest. The expansion rate gradually decreases to zero (at about 4.5 μs) as the rod passes and the cavity has expanded to its maximum radius (about 4.7 mm). The solid line in Fig. 7 represents a characteristic radial expansion history for the local cavity. This curve, based on the assumptions of constant local cavity shape and rod–plate interface velocity, was plotted from eqn (1) by varying the local cavity depth (z) from 0 to z_f as a function of time.

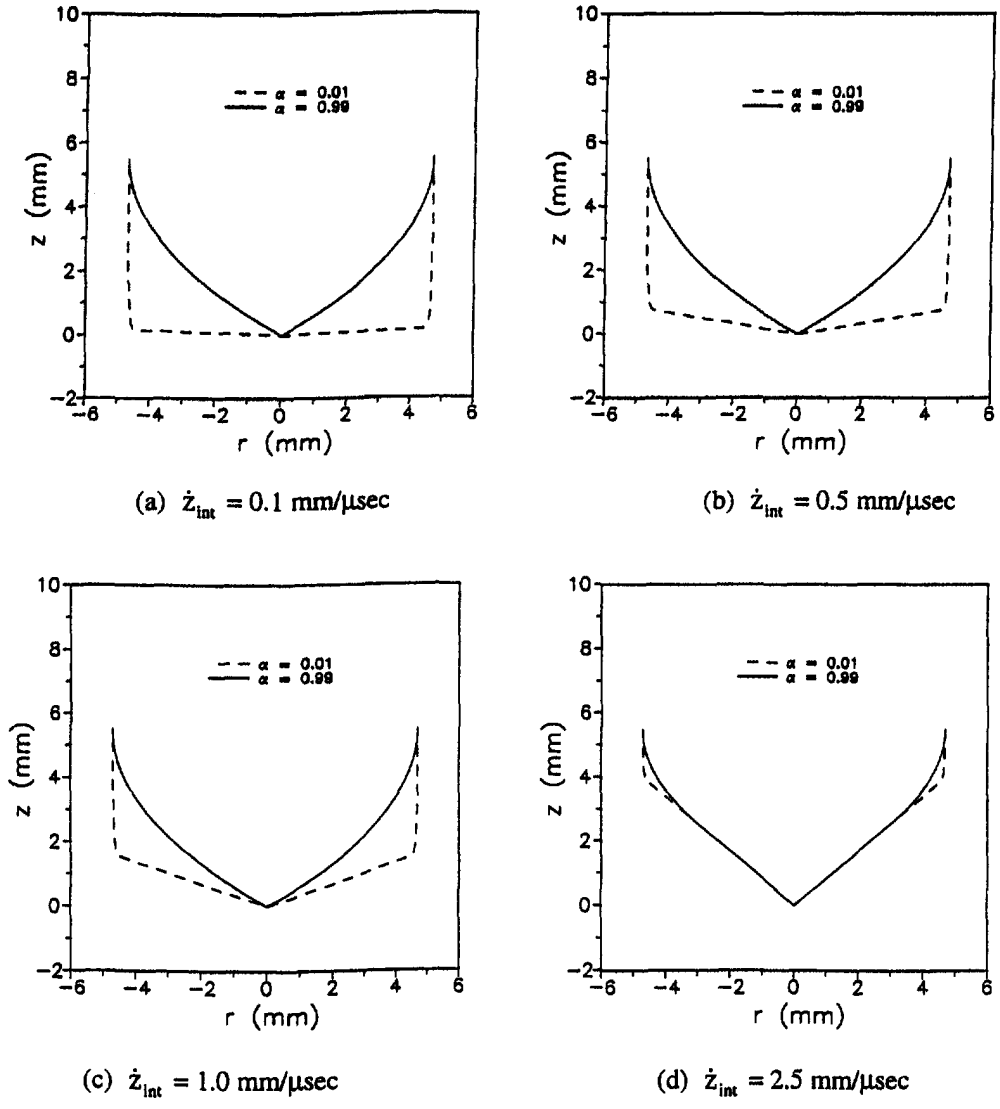

Fig. 4. Local cavity shape function for various values of $\dot{z}_{int}$ and α.

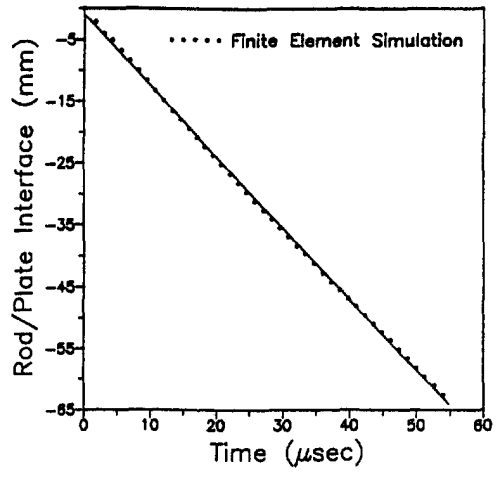

Fig. 5. Linear approximation to time history of rod–plate interface position from simulation of shot 4-1529.

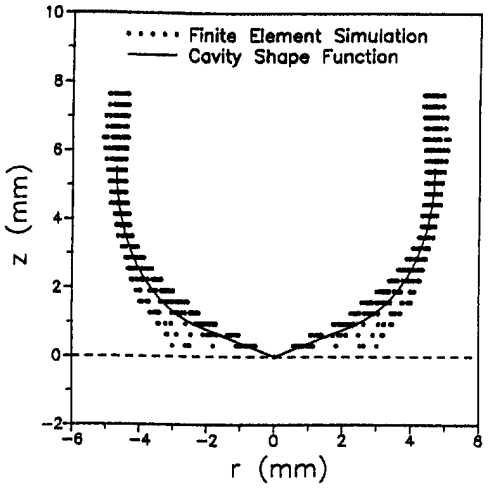

Fig. 6. Comparison of calibrated cavity shape function with data from simulation of shot 4-1529.

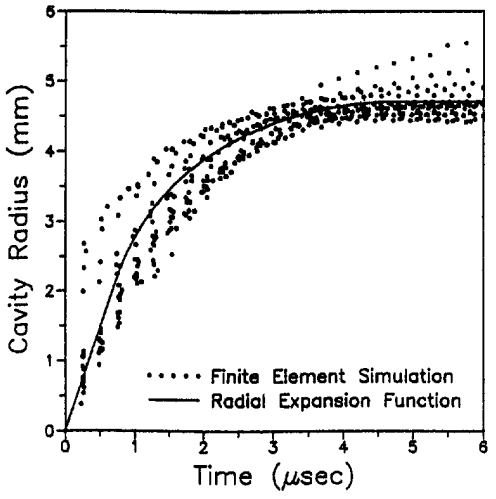

Fig. 7. Comparison of characteristic radial expansion function with data from simulation of shot 4-1529.

3.4. *Force–time history*

Methods to obtain accurate time histories of the forces exerted on targets from the above simulations were investigated. In one approach, the net system force exerted during a time step was determined by dividing the change in axial momentum by the time step ($\Delta M_z/\Delta t$). However, the resulting force–time history profile became extremely noisy after the first few microseconds; this was probably due to the simulated erosion process. To eliminate this noise problem, the simulated time history of the target plate's axial momentum was first approximated with a fifth-degree polynomial. The net axial force exerted on the target at any time could then be calculated from the polynomial's first derivative (dM_z/dt). The dashed line in Fig. 8 shows the smoothed axial force–time history that was computed from the simulation of shot 4-1529.

The other approach to find the instantaneous force exerted on the local cavity at any time during the penetration would be the product of the total pressure on the local cavity and the surface area of the local cavity. In evaluating the cavity's surface area, a numerical integration technique (e.g. the trapezoidal rule) is necessary to compute the surface area as a function of cavity depth. The local cavity's surface area varies with time. At the beginning of the rod penetration event there is no cavity, so the surface area is zero. As the penetration proceeds, the local cavity grows until it reaches its maximum depth, z_f. The surface area of the local cavity then remains constant until the global cavity depth equals the target plate's

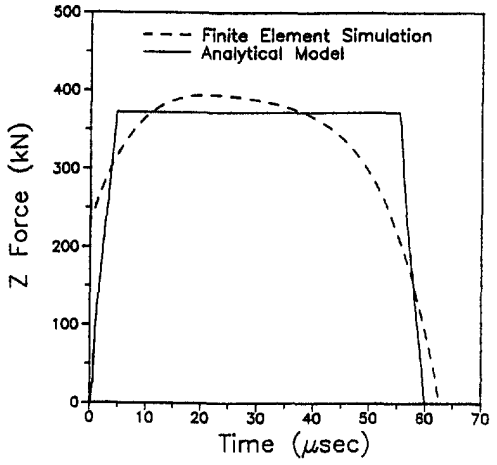

Fig. 8. Comparison of idealized force time history with data from simulation of shot 4-1529.

thickness. Finally, the local cavity's surface area decreases to zero as the projectile exits the target.

The total time-varying pressure, $P(t)$, exerted by the penetrating projectile into the target is the sum of the static pressure (P_S) and the dynamic pressure (P_D). For projectiles striking at low velocity, the static term is more dominant than the dynamic term, whereas for projectiles striking at high velocity the dynamic term is more dominant than the static term. An engineering model for the forces on rigid, long rods with spherical, ogival and conical noses that penetrated rate-independent, elastic–perfectly plastic targets was developed by Forrestal and Luk (1988). Forrestal *et al.* (1990) have used cylindrical cavity expansion and arrived at the expression for the static pressure (P_S) and the dynamic pressure (P_D) assuming an incompressible target with a power law strain hardening material. The above model describes the penetration of projectile for velocities less than 1.5 km s^{-1}. The only hypervelocity model available from a literature survey is given by Hanagud and Ross (1971). They showed the comparison between compressible and incompressible penetration theory for the hypervelocity impact of spherical steel projectiles on an aluminum target using spherical cavity expansion and deep penetration theory, and assumed a compressible target with a linear strain hardening material.

The static and dynamic pressure may be obtained from Forrestal and Luk (1988), Forrestal *et al.* (1990) and Hanagud and Ross (1971). The dynamic pressure term can be put in the form:

$$P_D = \bar{\beta}\dot{a}^2, \tag{3}$$

where $\bar{\beta}$ is a function of density and yield strength for a compressible or incompressible target material and $\dot{a}$ is the radial expansion velocity of the local cavity. Based on the assumptions that (a) the interface velocity remains constant and (b) the local cavity shape remains uniform throughout the penetration, then $\bar{\beta}$ may be considered to be a constant.

During the penetration event, the static pressure on the local cavity is constant and the dynamic pressure is a function of the local cavity's radial expansion rate. Within the local cavity, the radial expansion rate decreases from a maximum at the base to a minimum (zero) at the top; the dynamic pressure also varies along the wall of the local cavity. Based on the assumption of constant local cavity shape, the calculated distribution of dynamic pressure will remain constant throughout the penetration.

Calculation of force–time history in the second approach requires the local cavity shape parameters, the thickness of the target plate, the residual strength of the target and the parameter $\bar{\beta}$ used to compute the dynamic pressure. The solid line in Fig. 8 represents the force–time history that was computed for shot 4-1529. In this calculation, the local

cavity parameters given in Section 3.2 were used. The target plate was 63.5 mm thick and the dynamic pressure parameter $\bar{\beta}$ was set to 0.208 GPa μs^2 mm^{-2}. A static pressure of 2.08 GPa obtained from the simulation was considered. The loading history described by a dashed line has an idealized profile and is comparable to that from the finite element simulation.

4. CAVITY GROWTH AND EXPANSION MODEL

4.1. *Target material model in compression*

In the penetration problem the two heterogeneous bodies are in contact, one of which is the nose of a long rod cylindrical projectile, while the other is bounded by an axially-symmetric surface defined by the cavity shape function and is described in Section 3.2. Immediately upon impact, the projectile begins to penetrate the target. As the penetration proceeds, the projectile's nose remains in constant contact with the target and a cavity forms inside the target. This contact zone defines the target's local cavity. The target's local cavity is defined as that part of the global cavity in which radial expansion is occurring, i.e. in the immediate vicinity of the nose of the penetrating rod. Figure 9 describes the instantaneous local cavity growth in the axial direction given by eqn (1). A comparison with the finite element simulation is also shown. In this figure, μ represents dimensionless time $(= 1-\alpha)$. At $\mu = 1$, impact is about to occur, and the target surface is free of any local deformation or crater formation. When $\mu = 0$ the cavity is complete, and a new cavity starts forming. Defining the cavity growth process is a new concept. The formation of a complete cavity at $\mu = 0$ is also illustrated in Fig. 6.

In this paragraph, we explain the cavity expansion in the radial direction. The problem treated concerns a target material that experiences (a) ideal locking compressibility behavior under hydrostatic stress and (b) an elastic–plastic response represented by material octahedral shear stress–strain behavior (obtained from uniaxial compression test):

$$\tau_n = \begin{cases} E\dfrac{\gamma_n}{\sqrt{2}} & \text{for} \quad \tau_n < \dfrac{\sqrt{2}}{3}Y \\ \dfrac{\sqrt{2}}{3}Y\left[\left(1+\dfrac{E\gamma_n}{\sqrt{2}Y}\right)^N\right] & \text{for} \quad \tau_n \geqslant \dfrac{\sqrt{2}}{3}Y, \end{cases} \tag{4}$$

where E is the modulus of elasticity, Y is the dynamic yield strength of the target material

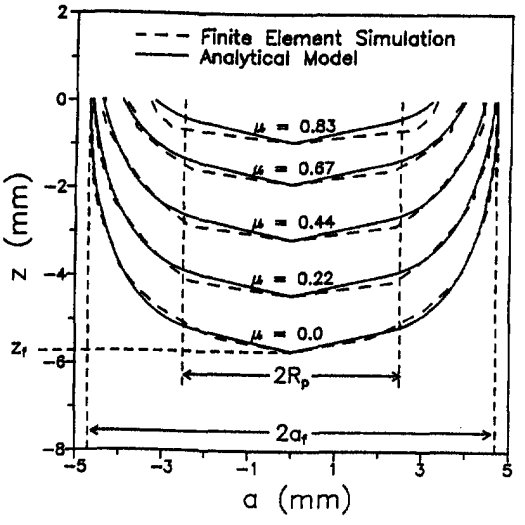

Fig. 9. Schematic of the local cavity growth in the axial direction.

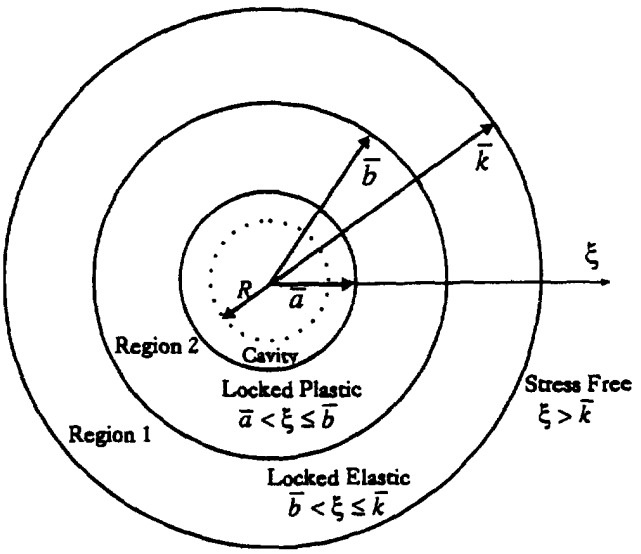

Fig. 10. Schematic of the cavity expansion in the radial direction.

and N is the strain hardening exponent. The octahedral shear stress τ_n is a function of effective stress $\bar{\sigma}$, and the octahedral shear strain γ_n is a function of effective strain $\bar{\varepsilon}$:

$$\tau_n = \frac{\sqrt{2}}{3}\bar{\sigma} \tag{5}$$

$$\gamma_n = \sqrt{2}\bar{\varepsilon}. \tag{6}$$

The relationship between stress and strain for an ideal plastic solid, with yielding caused by deviatoric stresses under uniaxial compression in plane strain, is given by the Levy–Mises criterion:

$$\sigma_z = \tfrac{1}{2}(\sigma_\theta + \sigma_r), \tag{7}$$

where σ_r, σ_θ and σ_z are the radial, circumferential and axial stresses, respectively, in the cylindrical coordinate (r, θ, z) system. Using eqns (4)–(7), the stress difference in the elastic and post-yield region is

$$\frac{\sigma_r - \sigma_\theta}{Y} = \begin{cases} \dfrac{2E}{\sqrt{3}Y}[(\varepsilon_r - \varepsilon_\theta)^2 + \varepsilon_\theta^2 + \varepsilon_r^2]^{1/2} & \text{elastic behavior} \\ \sqrt{\dfrac{2}{3}}\left\{1 + \left(\dfrac{2E}{3Y}\right)^N [(\varepsilon_r - \varepsilon_\theta)^2 + \varepsilon_\theta^2 + \varepsilon_r^2]^{\frac{N}{2}}\right\} & \text{post-yield behavior.} \end{cases} \tag{8}$$

The sudden application of pressure at the cavity surface in the initially stress-free solid in Fig. 10 produces a surrounding deformed region of material that is instantaneously elastic locked in dilatation and elastic in shear (Hanagud and Ross, 1971). In Fig. 10, $\bar{a} = (a/\dot{z}t)$, $\bar{b} = (b/\dot{z}t)$ and $\bar{k} = (k/\dot{z}t)$, where a is the radius of local cavity, b is the location of the elastic–plastic wave front, k is the location of the elastic wave front and $\dot{z}$ is the projectile–target interface velocity. The radial cavity expansion velocity is equal to the velocity of the wave in the plastic region.

The values of locking strain may be obtained from the experimental Rankine–Hugonoit relationship, which characterizes material behavior under hydrostatic compression at high rates of loading. The elastic situation persists under increasing pressure until yielding occurs at the cavity surface, whereupon the medium experiences plastic locking stress in dilatation

and plastic behavior in shear in the region $\bar{a} < \xi \leqslant \bar{b}$. At this point, values of hydrostatic stress for the locked plastic material are greater than those values characteristic of the locked elastic condition in the region $\bar{b} < \xi \leqslant \bar{k}$. Further increase of pressure with time causes the locked plastic region surrounding the cavity to grow in extent so that the surface which acts as a boundary between the initially generated locked elastic material and the following zone of locked plastic material, propagates outward radially from the expanding cavity surface.

The circumferential strain (ε_θ) and the hoop strain (ε_r) in terms of locking strain (ε_l) are (Managud and Ross, 1971):

$$\varepsilon_\theta = \ln\left[\frac{r}{r_0}\right] \quad \text{and} \quad \varepsilon_r = \varepsilon_l - 2\ln\left[\frac{r}{r_0}\right]. \tag{9}$$

Equation (8) in terms of locking strain gives

$$\frac{\sigma_r - \sigma_\theta}{Y} =$$

$$\begin{cases} \dfrac{2E}{\sqrt{3}Y}\left[\left\{3\ln\left(\dfrac{r}{r_0}\right)-\varepsilon_{lp}\right\}^2+\left\{\ln\left(\dfrac{r}{r_0}\right)\right\}^2+\left\{2\ln\left(\dfrac{r}{r_0}\right)-\varepsilon_{lp}\right\}^2\right]^{1/2} & \text{elastic behavior} \\ \sqrt{\dfrac{2}{3}}\left\{1+\left(\dfrac{2E}{3Y}\right)^N\left[\left\{3\ln\left(\dfrac{r}{r_0}\right)-\varepsilon_{lp}\right\}^2+\left\{\ln\left(\dfrac{r}{r_0}\right)\right\}^2+\left\{2\ln\left(\dfrac{r}{r_0}\right)-\varepsilon_{lp}\right\}^2\right]^{\frac{N}{2}}\right\} & \text{post-yield behavior.} \end{cases} \tag{10}$$

In eqns (9) and (10), r is the Eulerian radial coordinate, the subscript 0 represents initial value of particle position, ε_{lp} is the locked strain in the plastic region and ε_{le} is the locked strain in the elastic region.

4.2. *Formulation of motion of projectile in the stationary target*

A cavity expansion model is formulated using (a) the equation of mass conservation, (b) the equation of motion, (c) the constitutive equation and (d) particle wave velocity and displacement relationship.

The mass balance for a compressible solid is given by

$$\frac{\partial}{\partial r}(u_r - r)^2 = 2r\left(\frac{\rho_t}{\rho_0}\right) \tag{11}$$

and the radial component of the equation of motion or force balance is given by

$$\frac{\partial \sigma_r}{\partial r} + \frac{\sigma_r - \sigma_\theta}{r} = -\rho_t\left(\frac{\partial v_r}{\partial t} + v_r\frac{\partial v_r}{\partial r}\right). \tag{12}$$

Here, r is the location of the moving particle at time $t > 0$, u_r is the radial displacement at time $t > 0$, ρ_0 is the density of the target at time $t = 0$, ρ_t is the density of the target at time $t > 0$, σ_r and σ_θ are the radial and hoop components of Cauchy stress, and v_r is the particle velocity in the radial direction. The particle velocity and displacement are related by

$$v_r\left(1 + \frac{\partial u_r}{\partial r}\right) = \frac{\partial u_r}{\partial t}. \tag{13}$$

By solving eqns (11) and (13) the initial location of the moving particle or the shock front in the plastic and in the elastic region can be found. The initial location may be called the limit of integration and is denoted by η in eqn (14).

Now, introducing the dimensionless variables

$$S_1 = \frac{\sigma_r}{Y}, \quad S_2 = \frac{\sigma_\theta}{Y}, \quad \zeta_\xi = \frac{v_r}{\dot{z}}, \quad \bar{\eta} = \frac{\eta}{\dot{z}t}, \quad \gamma = \frac{u_r}{\dot{z}t} \tag{14}$$

and the similarity transformation

$$\xi = \frac{r}{\dot{z}t} \quad \text{and} \quad \xi_0 = \frac{r_0}{\dot{z}t} \tag{15}$$

in eqns (11) and (13) yields

$$\frac{\partial}{\partial \xi}(\xi - \gamma)^2 = 2\xi\left(\frac{\rho_l}{\rho_0}\right) \tag{16}$$

$$\zeta_\xi\left(1 - \frac{\mathrm{d}\gamma}{\mathrm{d}\xi}\right) = \gamma - \xi\frac{\mathrm{d}\gamma}{\mathrm{d}\xi}. \tag{17}$$

Integrating eqn (17) gives

$$\gamma = \xi - \sqrt{\frac{\rho_l}{\rho_0}(\xi^2 - \bar{\eta}^2)} \tag{18}$$

Substituting eqn (18) in eqn (16) gives

$$\zeta_\xi\left(\frac{\xi}{\sqrt{(\xi^2 - \bar{\eta}^2)}}\right) = -\sqrt{(\xi^2 - \bar{\eta}^2)} + \frac{\xi^2}{\sqrt{(\xi^2 - \bar{\eta}^2)}}, \tag{19}$$

which, upon simplification, gives the relation between particle velocity ζ_ξ and spatial displacement coordinate ξ:

$$\zeta_\xi = \frac{\bar{\eta}^2}{\xi}. \tag{20}$$

In Fig. 9, $\bar{a} = (a/\dot{z}t)$, $\bar{b} = (b/\dot{z}t)$ and $\bar{k} = (k/\dot{z}t)$, where a is the radius of the local cavity, b is the location of the elastic–plastic wave front, k is the location of the elastic wave front and $\dot{z}$ is the projectile–target interface velocity. The jump condition expressing the conservation of mass principle is applied on the shock front at the elastic–plastic interface:

$$\rho_{\mathrm{lp}}(\dot{\bar{b}} - \zeta_{\bar{b}}^{\mathrm{p}}) = \rho_{\mathrm{le}}(\dot{\bar{b}} - \zeta_{\bar{b}}^{\mathrm{e}}) \quad \text{at} \quad \xi = \bar{b}(t), \tag{21}$$

where ρ_{lp} and ρ_{le} are the locked plastic and elastic densities, respectively. The jump condition expressing the conservation of mass principle is applied on the shock front at the elastic and stress-free region:

$$\rho_0(\dot{\bar{k}} - \zeta_{\bar{k}}^0) = \rho_{\mathrm{le}}(\dot{\bar{k}} - \zeta_{\bar{k}}^{\mathrm{e}}) \quad \text{at} \quad \xi = \bar{k}(t). \tag{22}$$

In the above equation ρ_0 is the density of the target material at the stress free region. The particle velocity $\zeta_{\bar{k}}^0$ is zero in the stress free region, eqn (22) reduces to

$$\zeta_{\bar{k}}^{e} = \alpha_e \dot{\bar{k}}. \tag{23}$$

Using eqns (21) and (23), the particle velocity in the locked plastic region is determined:

$$\zeta_{\bar{b}}^{p} = \alpha_p \dot{\bar{b}} + (1-\alpha_p)\alpha_e \dot{\bar{k}}. \tag{24}$$

The initial location of the plastic shock front is obtained by substituting eqn (20) in eqn (24):

$$\dot{\bar{\eta}}_p = \sqrt{\alpha_p \bar{b}\dot{\bar{b}} + (1-\alpha_p)\alpha_e \bar{b}\dot{\bar{k}}}. \tag{25}$$

The initial location of the elastic shock front is obtained by substituting eqn (20) in eqn (24):

$$\dot{\bar{\eta}}_e = \sqrt{\alpha_e \bar{k}\dot{\bar{k}}}. \tag{26}$$

The time derivative of eqns (25) and (26) yields

$$\ddot{\bar{\eta}}_p = \frac{\alpha_p \bar{b}\ddot{\bar{b}} + \alpha_p \dot{\bar{b}}^2 + (1-\alpha_p)\alpha_e(\dot{\bar{k}}\dot{\bar{b}} + \bar{b}\ddot{\bar{k}})}{2\sqrt{\alpha_p \bar{b}\dot{\bar{b}} + (1-\alpha_p)\alpha_e \bar{b}\dot{\bar{k}}}} \tag{27}$$

$$\ddot{\bar{\eta}}_e = \left(\frac{\bar{k}\ddot{\bar{k}} + \dot{\bar{k}}^2}{2}\right)\sqrt{\frac{\alpha_e}{\bar{k}\dot{\bar{k}}}}. \tag{28}$$

In the above equations,

$$\alpha_e = \left(1 - \frac{\rho_0}{\rho_{1e}}\right) \quad \text{and} \quad \alpha_p = \left(1 - \frac{\rho_{1e}}{\rho_{1p}}\right). \tag{29}$$

Substituting eqns (14) and (15) in eqn (12) gives

$$\frac{dS_1}{d\xi} + \frac{S_1 - S_2}{\xi} = \frac{\rho_1 c^2}{Y}(\xi + \zeta_\xi)\frac{d\zeta_\xi}{d\xi}. \tag{30}$$

In the region $\bar{a} < \xi \leqslant \bar{b}$ of the plate target, the density and the strain are locked in plastic. Substituting eqns (14) and (15) in eqn (10) representing the post-yield behavior, we obtain

$$(S_1 - S_2) = \sqrt{\frac{2}{3}} + \left[\frac{2}{3}\right]^{N+1/2}\left(\frac{E}{Y}\right)^N \left[\left\{3\ln\left(\frac{\xi}{\xi_0}\right) - \varepsilon_{1p}\right\}^2 + \left\{\ln\left(\frac{\xi}{\xi_0}\right)\right\}^2 + \left\{2\ln\left(\frac{\xi}{\xi_0}\right) - \varepsilon_{1p}\right\}^2\right]^{\frac{N}{2}}. \tag{31}$$

Substituting eqn (31) in eqn (30), we get

$$\frac{dS_1^p}{d\xi} = -\frac{1}{\xi}\sqrt{\frac{2}{3}} - \left[\frac{2}{3}\right]^{N+1/2}\left(\frac{E}{Y}\right)^N \frac{1}{\xi}\left[\left\{3\ln\left(\frac{\xi}{\xi_0}\right) - \varepsilon_{lp}\right\}^2 + \left\{\ln\left(\frac{\xi}{\xi_0}\right)\right\}^2 + \left\{2\ln\left(\frac{\xi}{\xi_0}\right) - \varepsilon_{lp}\right\}^2\right]^{\frac{N}{2}} + \frac{\rho_{lp}c^2}{Y}(\xi + \zeta_\xi^p)\frac{d\zeta_\xi^p}{d\xi}. \quad (32)$$

On integrating eqn (32) from $\bar{\eta}_p$ to ξ,

$$S_1^p(\xi) = S_1^p(\bar{\eta}_p) - \left[\frac{2}{3}\right]^{N+1/2}\left(\frac{E}{Y}\right)^N \int_{\bar{\eta}_p}^{\xi} \frac{1}{\xi'}\left[\left\{3\ln\left(\frac{\xi'}{\xi_0}\right) - \varepsilon_{lp}\right\}^2 + \left\{\ln\left(\frac{\xi'}{\xi_0}\right)\right\}^2 + \left\{2\ln\left(\frac{\xi'}{\xi_0}\right) - \varepsilon_{lp}\right\}^2\right]^{\frac{N}{2}} d\xi' + \frac{\rho_{lp}c^2}{Y}\int_{\bar{\eta}_p}^{\xi}(\xi' + \zeta_{\xi'}^p)\frac{d\zeta_{\xi'}^p}{d\xi'}d\xi' - \sqrt{\frac{2}{3}}\int_{\bar{\eta}_p}^{\xi}\frac{1}{\xi'}d\xi', \quad (33)$$

gives

$$S_1^p(\xi) = S_1^p(\bar{\eta}_p) - \left[\frac{2}{3}\right]^{N+1/2}\left(\frac{E}{Y}\right)^N \int_{\bar{\eta}_p}^{\xi} \frac{1}{\xi'}\left[\left\{3\ln\left(\frac{\xi'}{\xi_0}\right) - \varepsilon_{lp}\right\}^2 + \left\{\ln\left(\frac{\xi'}{\xi_0}\right)\right\}^2 + \left\{2\ln\left(\frac{\xi'}{\xi_0}\right) - \varepsilon_{lp}\right\}^2\right]^{\frac{N}{2}} d\xi' - \frac{\rho_{lp}c^2}{2Y}\left(2\bar{\eta}_p^2\ln\frac{\xi}{\bar{\eta}_p} + \bar{\eta}_p^2 - \frac{\bar{\eta}_p^4}{\xi^2}\right) - \sqrt{\frac{2}{3}}\ln\frac{\xi}{\bar{\eta}_p}. \quad (34)$$

At $\xi = \bar{a}$, $S_1^p(\bar{a}) = \bar{S}_1(t)$,

$$S_1^p(\bar{\eta}_p) = \bar{S}_1(t) + \left[\frac{2}{3}\right]^{N+1/2}\left(\frac{E}{Y}\right)^N \int_{\bar{\eta}_p}^{\bar{a}} \frac{1}{\xi'}\left[\left\{3\ln\left(\frac{\xi'}{\xi_0}\right) - \varepsilon_{lp}\right\}^2 + \left\{\ln\left(\frac{\xi'}{\xi_0}\right)\right\}^2 + \left\{2\ln\left(\frac{\xi'}{\xi_0}\right) - \varepsilon_{lp}\right\}^2\right]^{\frac{N}{2}} d\xi' + \frac{\rho_{lp}c^2}{2Y}\left(2\bar{\eta}_p^2\ln\frac{\bar{a}}{\bar{\eta}_p} + \bar{\eta}_p^2 - \frac{\bar{\eta}_p^4}{\bar{a}^2}\right) + \sqrt{\frac{2}{3}}\ln\frac{\bar{a}}{\bar{\eta}_p}. \quad (35)$$

Substituting eqn (35) in eqn (34) gives the radial stress distribution in the region $\bar{a} < \xi \leqslant \bar{b}$, we get

$$S_1^p(\xi) = \bar{S}_1(t) - \left[\frac{2}{3}\right]^{N+1/2}\left(\frac{E}{Y}\right)^N \int_{a}^{\xi} \frac{1}{\xi'}\left[\left\{3\ln\left(\frac{\xi'}{\xi_0}\right) - \varepsilon_{lp}\right\}^2 + \left\{\ln\left(\frac{\xi'}{\xi_0}\right)\right\}^2 + \left\{2\ln\left(\frac{\xi'}{\xi_0}\right) - \varepsilon_{lp}\right\}^2\right]^{\frac{N}{2}} d\xi' - \frac{\rho_{lp}c^2}{Y}\left[2\bar{\eta}_p^2\left(\ln\frac{\xi}{\bar{\eta}_p} - \ln\frac{\bar{a}}{\bar{\eta}_p}\right) - \bar{\eta}_p^4\left(\frac{1}{\xi^2} - \frac{1}{\bar{a}^2}\right)\right] + \sqrt{\frac{2}{3}}\left(\ln\frac{\bar{a}}{\bar{\eta}_p} - \ln\frac{\xi}{\bar{\eta}_p}\right). \quad (36)$$

In the region $\bar{b} < \xi \leqslant \bar{k}$ of the plate target, the density and the strain are locked in elastic. Substituting eqns (14) and (15) in eqn (10) representing the elastic behavior yields

$$(S_1 - S_2) = \frac{2}{\sqrt{3}}\frac{E}{Y}\left[\left\{3\ln\left(\frac{\xi}{\xi_0}\right) - \varepsilon_{le}\right\}^2 + \left\{\ln\left(\frac{\xi}{\xi_0}\right)\right\}^2 + \left\{2\ln\left(\frac{\xi}{\xi_0}\right) - \varepsilon_{le}\right\}^2\right]^{1/2}. \quad (37)$$

Substituting eqn (37) in eqn (30) gives

$$\frac{dS_1^e}{d\xi} = -\frac{2}{\sqrt{3}\xi}\frac{E}{Y}\left[\left\{3\ln\left(\frac{\xi}{\xi_0}\right)-\varepsilon_{le}\right\}^2+\left\{\ln\left(\frac{\xi}{\xi_0}\right)\right\}^2+\left\{2\ln\left(\frac{\xi}{\xi_0}\right)-\varepsilon_{le}\right\}^2\right]^{1/2} + \frac{\rho_{lp}c^2}{Y}(\xi+\zeta_\xi^e)\frac{d\zeta_\xi^e}{d\xi}. \quad (38)$$

On integrating eqn (38) from $\bar{\eta}_e$ to ξ,

$$S_1^e(\xi) = S_1^e(\bar{\eta}_e) - \frac{2}{\sqrt{3}}\frac{E}{Y}\int_{\bar{\eta}_e}^{\xi}\frac{1}{\xi'}\left[\left\{3\ln\left(\frac{\xi'}{\xi_0}\right)-\varepsilon_{le}\right\}^2+\left\{\ln\left(\frac{\xi'}{\xi_0}\right)\right\}^2+\left\{2\ln\left(\frac{\xi'}{\xi_0}\right)-\varepsilon_{le}\right\}^2\right]^{1/2}d\xi' + \frac{\rho_{le}c^2}{Y}\int_{\bar{\eta}_e}^{\xi}(\xi'+\zeta_\xi^e)\frac{d\zeta_{\xi'}^e}{d\xi'}d\xi', \quad (39)$$

gives

$$S_1^e(\xi) = S_1^e(\bar{\eta}_e) - \frac{2}{\sqrt{3}}\frac{E}{Y}\int_{\bar{\eta}_e}^{\xi}\frac{1}{\xi'}\left[\left\{3\ln\left(\frac{\xi'}{\xi_0}\right)-\varepsilon_{le}\right\}^2+\left\{\ln\left(\frac{\xi'}{\xi_0}\right)\right\}^2+\left\{2\ln\left(\frac{\xi'}{\xi_0}\right)-\varepsilon_{le}\right\}^2\right]^{1/2}d\xi' - \frac{\rho_{le}c^2}{2Y}\left(2\bar{\eta}_e^2\ln\frac{\xi}{\bar{\eta}_e}+\bar{\eta}_e^2-\frac{\bar{\eta}_e^4}{\xi^2}\right). \quad (40)$$

In order to obtain the elastic integration constant $S_1^e(\bar{\eta}_e)$, the jump condition expressing the conservation of momentum principle is applied at the elastic–plastic interface $\xi = \bar{b}$:

$$S_1^p(\bar{b}) - S_1^e(\bar{b}) = -\frac{\rho_{lp}c^2}{Y}(\dot{\bar{b}}-\zeta_{\bar{b}}^p)\zeta_{\bar{b}}^p + \frac{\rho_{le}c^2}{Y}(\dot{\bar{b}}-\zeta_{\bar{b}}^e)\zeta_{\bar{b}}^e$$

$$= -\frac{\rho_{lp}c^2}{Y}[\dot{\bar{b}}-\alpha_p\dot{\bar{b}}-(1-\alpha_p)\alpha_e\dot{\bar{k}}](\alpha_p\dot{\bar{b}}+(1-\alpha_p)\alpha_e\dot{\bar{k}}) + \frac{\rho_{le}c^2}{Y}(\dot{\bar{b}}-\alpha_e\dot{\bar{k}})\alpha_e\dot{\bar{k}}. \quad (41)$$

Subtracting eqn (40) from eqn (36) and introducing $\xi = \bar{b}$, we obtain

$$S_1^p(\bar{b}) - S_1^e(\bar{b}) = \bar{S}_1(t) - \left[\frac{2}{3}\right]^{N+1/2}\left(\frac{E}{Y}\right)^N\int_a^{\bar{b}}\frac{1}{\xi'}\left[\left\{3\ln\left(\frac{\xi'}{\xi_0}\right)-\varepsilon_{lp}\right\}^2+\left\{\ln\left(\frac{\xi'}{\xi_0}\right)\right\}^2 + \left\{2\ln\left(\frac{\xi'}{\xi_0}\right)-\varepsilon_{lp}\right\}^2\right]^{\frac{N}{2}}d\xi' + \frac{2}{\sqrt{3}}\frac{E}{Y}\int_{\bar{\eta}_e}^{\bar{b}}\frac{1}{\xi'}\left[\left\{3\ln\left(\frac{\xi'}{\xi_0}\right)-\varepsilon_{le}\right\}^2+\left\{\ln\left(\frac{\xi'}{\xi_0}\right)\right\}^2 + \left\{2\ln\left(\frac{\xi'}{\xi_0}\right)-\varepsilon_{le}\right\}^2\right]^{1/2}d\xi' - S_1^e(\bar{\eta}_e) - \frac{\rho_{lp}c^2}{2Y}\left[2\bar{\eta}_p^2\left(\ln\frac{\bar{b}}{\bar{\eta}_p}-\ln\frac{\bar{a}}{\bar{\eta}_p}\right)-\bar{\eta}_p^4\left(\frac{1}{\bar{b}^2}-\frac{1}{\bar{a}^2}\right)\right] + \sqrt{\frac{2}{3}}\left(\ln\frac{\bar{a}}{\bar{\eta}_p}-\ln\frac{\bar{b}}{\bar{\eta}_p}\right)+\frac{\rho_{le}c^2}{2Y}\left(2\bar{\eta}_e^2\ln\frac{\bar{b}}{\bar{\eta}_e}+\bar{\eta}_e^2-\frac{\bar{\eta}_e^4}{\bar{b}^2}\right). \quad (42)$$

Substituting eqn (41) in eqn (40) gives the elastic integration constant $S_1^e(\bar{\eta}_e)$:

$$S_1^e(\bar{\eta}_e) = \bar{S}_1(t) - \left[\frac{2}{3}\right]^{N+1/2}\left(\frac{E}{Y}\right)^N \int_a^{\bar{b}} \frac{1}{\xi'}\left[\left\{3\ln\left(\frac{\xi'}{\xi_0}\right) - \varepsilon_{lp}\right\}^2 + \left\{\ln\left(\frac{\xi'}{\xi_0}\right)\right\}^2 + \left\{2\ln\left(\frac{\xi'}{\xi_0}\right) - \varepsilon_{lp}\right\}^2\right]^{\frac{N}{2}} d\xi' + \frac{2}{\sqrt{3}}\frac{E}{Y}\int_{\bar{\eta}_e}^{\bar{b}} \frac{1}{\xi'}\left[\left\{3\ln\left(\frac{\xi'}{\xi_0}\right) - \varepsilon_{le}\right\}^2 + \left\{\ln\left(\frac{\xi'}{\xi_0}\right)\right\}^2 + \left\{2\ln\left(\frac{\xi'}{\xi_0}\right) - \varepsilon_{le}\right\}^2\right]^{1/2} d\xi' + \sqrt{\frac{2}{3}}\left(\ln\frac{\bar{a}}{\bar{\eta}_p} - \ln\frac{\bar{b}}{\bar{\eta}_p}\right) - \frac{\rho_{lp}c^2}{2Y}\left[2\bar{\eta}_p^2\left(\ln\frac{\bar{b}}{\bar{\eta}_p} - \ln\frac{\bar{a}}{\bar{\eta}_p}\right) - \bar{\eta}_p^4\left(\frac{1}{\bar{b}^2} - \frac{1}{\bar{a}^2}\right)\right] + \frac{\rho_{le}c^2}{2Y}\left(2\bar{\eta}_e^2\ln\frac{\bar{b}}{\bar{\eta}_e} + \bar{\eta}_e^2 - \frac{\bar{\eta}_e^4}{\bar{b}^2}\right) + \frac{\rho_{lp}c^2}{Y}[\dot{\bar{b}} - \alpha_p\dot{\bar{b}} - (1-\alpha_p)\alpha_e\dot{\bar{k}}](\alpha_p\dot{\bar{b}} + (1-\alpha_p)\alpha_e\dot{\bar{k}}) - \frac{\rho_{le}c^2}{Y}(\dot{\bar{b}} - \alpha_e\dot{\bar{k}})\alpha_e\dot{\bar{k}}. \tag{43}$$

Substituting eqn (43) in eqn (40) gives the radial stress distribution in the region $\bar{a} < \xi \leqslant \bar{b}$:

$$S_1^e(\xi) = \bar{S}_1(t) - \left[\frac{2}{3}\right]^{N+1/2}\left(\frac{E}{Y}\right)^N \int_a^{\bar{b}} \frac{1}{\xi'}\left[\left\{3\ln\left(\frac{\xi'}{\xi_0}\right) - \varepsilon_{lp}\right\}^2 + \left\{\ln\left(\frac{\xi'}{\xi_0}\right)\right\}^2 + \left\{2\ln\left(\frac{\xi'}{\xi_0}\right) - \varepsilon_{lp}\right\}^2\right]^{\frac{N}{2}} d\xi' - \frac{2}{\sqrt{3}}\frac{E}{Y}\int_{\bar{b}}^{\xi} \frac{1}{\xi'}\left[\left\{3\ln\left(\frac{\xi'}{\xi_0}\right) - \varepsilon_{le}\right\}^2 + \left\{\ln\left(\frac{\xi'}{\xi_0}\right)\right\}^2 + \left\{2\ln\left(\frac{\xi'}{\xi_0}\right) - \varepsilon_{le}\right\}^2\right]^{1/2} d\xi' + \sqrt{\frac{2}{3}}\left(\ln\frac{\bar{a}}{\bar{\eta}_p} - \ln\frac{\bar{b}}{\bar{\eta}_p}\right) - \frac{\rho_{lp}c^2}{Y}\left[2\bar{\eta}_p^2\left(\ln\frac{\bar{b}}{\bar{\eta}_p} - \ln\frac{\bar{a}}{\bar{\eta}_p}\right) - \bar{\eta}_p^4\left(\frac{1}{\bar{b}} - \frac{1}{\bar{a}^2}\right)\right] - \frac{\rho_{le}c^2}{Y}\left[2\bar{\eta}_e^2\left(\ln\frac{\xi}{\bar{\eta}_e} - \ln\frac{\bar{b}}{\bar{\eta}_e}\right) - \bar{\eta}_e^4\left(\frac{1}{\xi^2} - \frac{1}{\bar{b}^2}\right)\right] + \frac{\rho_{lp}c^2}{Y}[\dot{\bar{b}} - \alpha_p\dot{\bar{b}} - (1-\alpha_p)\alpha_e\dot{\bar{k}}](\alpha_p\dot{\bar{b}} + (1-\alpha_p)\alpha_e\dot{\bar{k}}) - \frac{\rho_{le}c^2}{Y}\rho_{le}(\dot{\bar{b}} - \alpha_e\dot{\bar{k}})\alpha_e\dot{\bar{k}}. \tag{44}$$

In the region $\bar{k} < \xi \leqslant \bar{o}$ of the plate target, the density and strain are not locked. The jump condition expressing the conservation of momentum principle is applied at the elastic stress-free interface:

$$S_1^e(\bar{k}) - S_1^e(o) = -\frac{\rho_{le}c^2}{Y}(\dot{\bar{k}} - \zeta_k^e)\zeta_k^e + \frac{\rho_0 c^2}{Y}(\dot{\bar{k}} - \zeta_k^0)\zeta_k^0. \tag{45}$$

At the stress-free region $S_1^e(\bar{o}) \approx 0$, from which the elastic radial stress at $\xi = \bar{k}$ is

$$S_1^e(\bar{k}) - S_1^e(o) = -\frac{\rho_{le}c^2}{Y}(\dot{\bar{k}} - \alpha_e\dot{\bar{k}})\alpha_e\bar{k}. \tag{46}$$

From eqns (44) and (46) at $\xi = \bar{k}$, an expression for the time variation of normalized radial stress distribution from $\bar{a} \leqslant \xi \leqslant \bar{k}$ results:

$$\bar{S}_1(t) = \left[\frac{2}{3}\right]^{N+1/2}\left(\frac{E}{Y}\right)^N \int_a^b \frac{1}{\xi'}\left[\left\{3\ln\left(\frac{\xi'}{\xi_0}\right)-\varepsilon_{lp}\right\}^2+\left\{\ln\left(\frac{\xi'}{\xi_0}\right)\right\}^2\right.$$
$$\left.+\left\{2\ln\left(\frac{\xi'}{\xi_0}\right)-\varepsilon_{lp}\right\}^2\right]^{\frac{N}{2}} d\xi' + \frac{2}{\sqrt{3}}\frac{E}{Y}\int_b^k \frac{1}{\xi'}\left[\left\{3\ln\left(\frac{\xi'}{\xi_0}\right)-\varepsilon_{le}\right\}^2+\left\{\ln\left(\frac{\xi'}{\xi_0}\right)\right\}^2\right.$$
$$\left.+\left\{2\ln\left(\frac{\xi'}{\xi_0}\right)-\varepsilon_{le}\right\}^2\right]^{1/2} d\xi' + \frac{\rho_{lp}c^2}{2Y}\left[2\bar{\eta}_p^2\left(\ln\frac{\bar{b}}{\bar{\eta}_p}-\ln\frac{\bar{a}}{\bar{\eta}_p}\right)-\bar{\eta}_p^4\left(\frac{1}{\bar{b}^2}-\frac{1}{\bar{a}^2}\right)\right]$$
$$+\frac{\rho_{le}c^2}{2Y}\left[2\bar{\eta}_e^2\left(\ln\frac{\bar{k}}{\bar{\eta}_e}-\ln\frac{\bar{b}}{\bar{\eta}_e}\right)-\bar{\eta}_e^4\left(\frac{1}{\bar{k}^2}-\frac{1}{\bar{b}^2}\right)\right]$$
$$-\frac{\rho_{lp}c^2}{Y}[\dot{\bar{b}}-\alpha_p\dot{\bar{b}}-(1-\alpha_p)\alpha_e\dot{\bar{k}}](\alpha_p\dot{\bar{b}}+(1-\alpha_p)\alpha_e\dot{\bar{k}})$$
$$+\frac{\rho_{le}c^2}{Y}(\dot{\bar{b}}-\dot{\bar{k}})\alpha_e\dot{\bar{k}}-\sqrt{\frac{2}{3}}\left(\ln\frac{\bar{a}}{\bar{\eta}_p}-\ln\frac{\bar{b}}{\bar{\eta}_p}\right). \tag{47}$$

It is apparent that the static and dynamic stress terms in eqn (47) can be separated, and for this purpose it is convenient to represent static terms by the quantity $\bar{S}_{1(s)}$, where

$$\bar{S}_{1(s)} = \left[\frac{2}{3}\right]^{N+1/2}\left(\frac{E}{Y}\right)^N \int_a^b \frac{1}{\xi'}\left[\left\{3\ln\left(\frac{\xi'}{\xi_0}\right)-\varepsilon_{lp}\right\}^2+\left\{\ln\left(\frac{\xi'}{\xi_0}\right)\right\}^2+\left\{2\ln\left(\frac{\xi'}{\xi_0}\right)-\varepsilon_{lp}\right\}^2\right]^{\frac{N}{2}} d\xi'$$
$$+\frac{2}{\sqrt{3}}\frac{E}{Y}\int_b^k \frac{1}{\xi'}\left[\left\{3\ln\left(\frac{\xi'}{\xi_0}\right)-\varepsilon_{le}\right\}^2+\left\{\ln\left(\frac{\xi'}{\xi_0}\right)\right\}^2+\left\{2\ln\left(\frac{\xi'}{\xi_0}\right)-\varepsilon_{le}\right\}^2\right]^{1/2} d\xi' - \sqrt{\frac{2}{3}}\ln\frac{\bar{a}}{\bar{b}} \tag{48}$$

and the dynamic term by the quantity $\bar{S}_{1(D)}$:

$$\bar{S}_{1(D)} = \frac{\rho_{lp}c^2}{2Y}\left[2\bar{\eta}_p^2\ln\frac{\bar{b}}{\bar{a}}-\bar{\eta}_p^4\left(\frac{\bar{a}^2}{\bar{b}^2}-1\right)\frac{1}{\bar{a}^2}\right]+\frac{\rho_{le}c^2}{2Y}\left[2\bar{\eta}_e^2\ln\frac{\bar{k}}{\bar{b}}-\bar{\eta}_e^4\left(\frac{\bar{b}^2}{\bar{k}^2}-1\right)\frac{1}{\bar{b}^2}\right]$$
$$-\frac{\rho_{lp}c^2}{Y}[\dot{\bar{b}}-\alpha_p\dot{\bar{b}}-(1-\alpha_p)\alpha_e\dot{\bar{k}}](\alpha_p\dot{\bar{b}}+(1-\alpha_p)\alpha_e\dot{\bar{k}})+\frac{\rho_{le}c^2}{Y}(\dot{\bar{b}}-\dot{\bar{k}})\alpha_e\dot{\bar{k}}. \tag{49}$$

In order to solve eqns (48) and (49) we need to find the relation between $\bar{a}$ and $\bar{b}$ and their time derivatives. At the yield point for $N = 0$ in eqn (10), characterizing the yield point of the target material:

$$(S_1^e - S_2^e) = \frac{2\sqrt{2}}{\sqrt{3}} \tag{50}$$

and for the elastic region $\bar{b} < \xi \leqslant \bar{k}$

$$(S_1^e - S_2^e) = \frac{2}{\sqrt{3}}\frac{E}{Y}\left[\left\{3\ln\left(\frac{\xi}{\xi_0}\right)-\varepsilon_{le}\right\}^2+\left\{\ln\left(\frac{\xi}{\xi_0}\right)\right\}^2+\left\{2\ln\left(\frac{\xi}{\xi_0}\right)-\varepsilon_{le}\right\}^2\right]^{1/2}. \tag{51}$$

Using eqns (50) and (51), at $\xi = \bar{b}$:

$$2\left(\frac{Y}{E}\right)^2 = \left[\left\{3\ln\left(\frac{b}{b_0}\right)-\varepsilon_{le}\right\}^2 + \left\{\ln\left(\frac{b}{b_0}\right)\right\}^2 + \left\{2\ln\left(\frac{b}{b_0}\right)-\varepsilon_{le}\right\}^2\right] \tag{52}$$

and at $\xi = \bar{a}$:

$$2\left(\frac{Y}{E}\right)^2 \leqslant \left[\left\{3\ln\left(\frac{a}{a_0}\right)-\varepsilon_{lp}\right\}^2 + \left\{\ln\left(\frac{a}{a_0}\right)\right\}^2 + \left\{2\ln\left(\frac{a}{a_0}\right)-\varepsilon_{lp}\right\}^2\right]. \tag{53}$$

In eqns (52) and (53), a_0 and b_0 are the initial values of the plastic and elastic–plastic wave fronts. The initial value of a_0 may be considered as the radius of the projectile.

For simplification let $\ln(a/a_0) = \beta'$ and $\ln(b/b_0) = \delta'$, then it follows that

$$a = a_0\,e^{\beta'}, \quad b = b_0\,e^{\delta'}. \tag{54}$$

Substituting eqn (54) in eqns (52) and (53) gives

$$2\left(\frac{Y}{E}\right)^2 = [(3\delta'-\varepsilon_{le})^2 + \delta'^2 + (2\delta'-\varepsilon_{le})^2]$$

$$\left(\frac{Y}{E}\right)^2 \leqslant [(3\beta'-\varepsilon_{lp})^2 + \beta'^2 + (2\beta'-\varepsilon_{lp})^2]. \tag{55}$$

From eqn (55) δ' and β' can be estimated for a given Y, E, ε_{le} and ε_{lp}. ε_{le} and ε_{lp} are to be obtained from the Huguenot curve for any isotropic target material. It is assumed that the leading shock front at $\xi = \bar{k}$ is relatively weak, such that the elastic locking strain ε_{le} and concomitant jump in density from the stress-free region to the locked elastic region are very small, then it follows that $\varepsilon_{le} = 0$ and $\rho_{le} = 0$. So, the first expression of eqn (55) gives

$$\delta' = 0.378\left(\frac{Y}{E}\right). \tag{56}$$

Equations (25) and (27) give

$$\bar{\eta}_P = \sqrt{\alpha_p \bar{b}\dot{\bar{b}}} \quad \text{and} \quad \dot{\bar{\eta}}_p = \frac{\alpha_p[(\bar{b}\ddot{\bar{b}}) + \dot{\bar{b}}^2]}{2\sqrt{\alpha_p \bar{b}\dot{\bar{b}}}}, \tag{57}$$

and eqns (26) and (28) result in $\bar{\eta} = 0$ and $\dot{\bar{\eta}} = 0$. Also, from eqn (21), at $\xi = \bar{a}$, the particle velocity ζ_a is equal to the cavity expansion velocity $\dot{\bar{a}}$. The cavity expansion front is given by

$$\bar{\eta}_p^2 = \bar{a}\dot{\bar{a}}. \tag{58}$$

Substituting eqn (58) in eqn (57) gives

$$\dot{\bar{b}} = \frac{\dot{\bar{a}}}{\alpha_p}\left(\frac{\bar{a}}{\bar{b}}\right). \tag{59}$$

We consider the compressibility in the locked plastic region, $\bar{a} < \xi \leqslant \bar{b}$, over an arbitrary

time period $t' = t_0$ ($\bar{a}' = \bar{a}_0, \xi' = \xi_0$) and $t' = t$ ($\bar{a}' = \bar{a}; \xi' = \xi$). Applying mass conservation,

$$(\xi^3 - \bar{a}^3)\rho_{lp} = (\xi_0^3 - \bar{a}_0^3)\rho_{le}, \tag{60}$$

gives

$$\ln\left(\frac{\xi}{\xi_0}\right) = -\tfrac{1}{3}\ln\left[1 - \left(\frac{\bar{a}}{\xi}\right)^3 + \left((1-\alpha_p)\left(\frac{\bar{a}}{\xi}\right)^3 e^{-3\beta'}\right)\right] + \tfrac{1}{3}\ln(1-\alpha_p). \tag{61}$$

Replacing ξ and ξ_0 by $\bar{b}$ and $\bar{b}_0$, respectively, in eqn (61) gives

$$\bar{b} = \bar{a}\sqrt[3]{\frac{1-e^{-3\beta'}(1-\alpha_p)}{1-e^{-3\delta'}(1-\alpha_p)}} \quad \text{and} \quad \dot{\bar{a}} = \dot{\bar{b}}\sqrt[3]{\frac{1-e^{-3\beta'}(1-\alpha_p)}{1-e^{-3\delta'}(1-\alpha_p)}}. \tag{62}$$

4.3. *Evaluation of the static and dynamic hoop stress*

We consider the compressibility in the locked elastic region, $\bar{b} < \xi \leqslant \bar{k}$, $t' = t_0$ ($\bar{b}' = \bar{b}_0, \xi' = \xi_0$) and $t' = t$ ($\bar{b}' = \bar{b}, \xi' = \xi$). Applying mass conservation,

$$(\xi^3 - \bar{b}^3)\rho_{le} = (\xi_0^3 - \bar{b}_0^3)\rho_0, \tag{63}$$

gives

$$\ln\left(\frac{\xi}{\xi_0}\right) = -\tfrac{1}{3}\ln\left[1 - \left(\frac{\bar{b}}{\xi}\right)^3 + \left((1-\alpha_e)\left(\frac{\bar{b}}{\xi}\right)^3 e^{-3\delta'}\right)\right] + \tfrac{1}{3}\ln(1-\alpha_e). \tag{64}$$

For a weak shock load at $\bar{b} < \xi \leqslant \bar{k}$, $\varepsilon_{le} \approx 0$, $\rho_0 = \rho_{le}$ and $\alpha_e = 0$, eqn (64) gives

$$\left(\frac{\xi}{\xi_0}\right) = \left[1 + e^{-3\delta'}\left(\frac{\bar{b}}{\xi}\right)^3 - \left(\frac{\bar{b}}{\xi}\right)^3\right]^{-1/3}. \tag{65}$$

The expansion series for $e^{-3\delta'}$ is

$$e^{-3\delta'} = 1 - 3\delta' + \tfrac{9}{2}\delta'^2 - \tfrac{27}{6}\delta'^3 + \ldots \tag{66}$$

Using eqns (65) and (66), we obtain

$$\left(\frac{\xi}{\xi_0}\right) = \left[1 - \left(\frac{\bar{b}}{\xi}\right)^3 (3\delta' - \tfrac{9}{2}\delta'^2 + \tfrac{27}{6}\delta'^3 \ldots)\right]^{-1/3}. \tag{67}$$

The expansion series for $\ln(1+x)$ is

$$\ln(1+x) = [x - \tfrac{1}{2}x^2 + \tfrac{1}{3}x^3 - \tfrac{1}{4}x^4 + \ldots]. \tag{68}$$

Making use of eqns (67) and (68) gives

$$\ln\left(\frac{\xi}{\xi_0}\right) = -\frac{1}{3}\left\{\left(\frac{\bar{b}}{\xi}\right)^3(-3\delta' + \tfrac{9}{2}\delta'^2 - \tfrac{27}{6}\delta'^3 + \ldots) + \frac{1}{2}\left[\left(\frac{\bar{b}}{\xi}\right)^3(-3\delta' + \tfrac{9}{2}\delta'^2 - \tfrac{27}{6}\delta'^3 + \ldots)\right]^2 + \ldots\right\}. \quad (69)$$

For $\delta' \ll 1$, this results in

$$\ln\left(\frac{\xi}{\xi_0}\right) = \frac{1}{3}\left\{\left(\frac{\bar{b}}{\xi}\right)^3(3\delta' - \tfrac{9}{2}\delta'^2 + \tfrac{27}{6}\delta'^3 \ldots)\right\}. \quad (70)$$

Using eqn (70), the elastic integral term in eqn (48) is

$$\frac{2}{\sqrt{3}}\frac{E}{Y}\int_{\bar{b}}^{k}\frac{1}{\xi'}\left[\left\{3\ln\left(\frac{\xi'}{\xi_0}\right) - \varepsilon_{le}\right\}^2 + \left\{\ln\left(\frac{\xi'}{\xi_0}\right)\right\}^2 + \left\{2\ln\left(\frac{\xi'}{\xi_0}\right) - \varepsilon_{le}\right\}^2\right]^{1/2} d\xi'$$

$$= \frac{2}{\sqrt{3}}\frac{E}{Y}\int_{\bar{b}}^{k}\frac{1}{\xi'}\left[\frac{\sqrt{14}}{3}\left(\frac{\bar{b}}{\xi'}\right)^3(3\delta' - \tfrac{9}{2}\delta'^2 + \ldots)\right]d\xi'$$

$$= -\frac{2\sqrt{42}}{27}\frac{E}{Y}\bar{b}^3(1-e^{-3\delta'})\left(\frac{1}{\bar{k}^3} - \frac{1}{\bar{b}^3}\right) = 0.48\frac{E}{Y}(1-e^{-3\delta'}) \quad \text{for } k \to \infty. \quad (71)$$

The term $\sqrt{2/3}\ln(\bar{a}/\bar{b})$ in eqn (48) is obtained from eqn (62) as

$$\sqrt{\frac{2}{3}}\ln\frac{\bar{a}}{\bar{b}} = 0.272\ln\left[\frac{1-e^{-3\delta'}(1-\alpha_p)}{1-e^{-3\beta'}(1-\alpha_p)}\right]. \quad (72)$$

The static pressure term given by eqn (48) is

$$\bar{S}_{1(s)} = \left[\frac{2}{3}\right]^{N+1/2}\left(\frac{E}{Y}\right)^N\int_a^{\bar{b}}\frac{1}{\xi'}\left[\left\{3\ln\left(\frac{\xi'}{\xi_0}\right) - \varepsilon_{lp}\right\}^2 + \left\{\ln\left(\frac{\xi'}{\xi_0}\right)\right\}^2 + \left\{2\ln\left(\frac{\xi'}{\xi_0}\right) - \varepsilon_{lp}\right\}^2\right]^{N/2} d\xi'$$

$$+0.48\frac{E}{Y}(1-e^{-3\delta'}) - 0.272\ln\left[\frac{1-e^{-3\delta'}(1-\alpha_p)}{1-e^{-3\beta'}(1-\alpha_p)}\right]. \quad (73)$$

Equation (73) also represents the residual strength of the target. For incompressible solid, $\rho_0 \approx \rho_{le} \approx \rho_{lp}$, $\varepsilon_{le} = \varepsilon_{lp} = 0$, the static pressure term in eqn (73) is

$$\bar{S}_{1(s)} = \frac{\sqrt{14^N}}{N+1}\left[\ln\left(\frac{1-e^{-3\beta'}}{1-e^{-3\delta'}}\right)^{N+1}\right] + 0.48\frac{E}{Y}(1-e^{-3\delta'}) - 0.272\ln\left[\frac{1-e^{-3\delta'}}{1-e^{-3\beta'}}\right]. \quad (74)$$

The dynamic term $\bar{S}_{1(D)}$ in eqn (49) is given by

$$\bar{S}_{1(D)} = -\frac{\rho_{lp}c^2}{2Y}\left[\tfrac{2}{3}(\bar{a}\dot{\bar{a}})\ln\left\{\frac{1-e^{-3\delta'}(1-\alpha_p)}{1-e^{-3\beta'}(1-\alpha_p)}\right\} + \dot{\bar{a}}^2\left\{\frac{1-e^{-3\delta'}(1-\alpha_p)}{1-e^{-3\beta'}(1-\alpha_p)}\right\}^{2/3} - \dot{\bar{a}}^2\right]. \quad (75)$$

For an incompressible solid, $\rho_0 \approx \rho_{le} \approx \rho_{lp}$, $\varepsilon_{le} = \varepsilon_{lp} = 0$, $\alpha_p = 0$, it follows from eqn (75) that

$$\bar{S}_{1(D)} = -\frac{\rho_0 c^2}{2Y}\left[\tfrac{2}{3}(\bar{a}\dot{\bar{a}})\ln\left\{\frac{1-e^{-3\delta'}}{1-e^{-3\beta'}}\right\}+\dot{\bar{a}}^2\left\{\left(\frac{1-e^{-3\delta'}}{1-e^{-3\beta'}}\right)^{2/3}-1\right\}\right]. \tag{76}$$

The final expression for the time-varying normalized radial stress distribution is

$$\bar{S}_1(t) = \frac{\sqrt{14^N}}{N+1}\left[\ln\left(\frac{1-e^{-3\beta'}}{1-e^{-3\delta'}}\right)^{N+1}\right]+0.48\frac{E}{Y}(1-e^{-3\delta'})-0.272\ln\left[\frac{1-e^{-3\delta'}}{1-e^{-3\beta'}}\right]$$
$$-\frac{\rho_0 c^2}{2Y}\left[\tfrac{2}{3}(\bar{a}\dot{\bar{a}})\ln\left\{\frac{1-e^{-3\delta'}}{1-e^{-3\beta'}}\right\}+\dot{\bar{a}}^2\left\{\left(\frac{1-e^{-3\delta'}}{1-e^{-3\beta'}}\right)^{2/3}-1\right\}\right]. \tag{77}$$

4.4. *Pressure distribution on the cavity wall*

The time-varying pressure $P(t)$ acting on the cavity is

$$\bar{P}(t) = \tfrac{1}{3}(\bar{S}_1+\bar{S}_2+\bar{S}_3). \tag{78}$$

In an axisymmetric plane strain problem, $\bar{S}_2 = 0$ and $\bar{S}_3 = (1/2)\bar{S}_1$. The expression for time-varying pressure is

$$\bar{P}(t) = \frac{1}{2}\left\{\frac{\sqrt{14^N}}{N+1}\left[\ln\left(\frac{1-e^{-3\beta'}}{1-e^{-3\delta'}}\right)^{N+1}\right]+0.48\frac{E}{Y}(1-e^{-3\delta'})-0.272\ln\left[\frac{1-e^{-3\delta'}}{1-e^{-3\beta'}}\right]\right\}$$
$$-\frac{\rho_0 c^2}{4Y}\left[\tfrac{2}{3}(\bar{a}\dot{\bar{a}})\ln\left\{\frac{1-e^{-3\delta'}}{1-e^{-3\beta'}}\right\}+\dot{\bar{a}}^2\left\{\left(\frac{1-e^{-3\delta'}}{1-e^{-3\beta'}}\right)^{2/3}-1\right\}\right]. \tag{79}$$

4.5. *Force–time history for the penetration event*

The time-varying pressure multiplied by the time-varying surface area results in force–time history of the penetrating projectile in a thick target:

$$F(r,z,t) = Y\bar{P}(t)\int_0^{z_f}\int_0^{a_f} 2\pi a(z)\,dr\,dz. \tag{80}$$

5. INFLUENCE OF TARGET THICKNESS AND STRIKING VELOCITY OF THE PROJECTILE

Using the material properties for the target and the projectile (given in Table 4), in eqns (1) and (80) the force time history is obtained for the penetration event. Table 5 illustrates the influence of target thickness and striking velocity of the projectile on the characteristic force time history. Also superimposed is the initial momentum of the projectile, and momentum transferred by the projectile to the target. The first column describes the striking velocity of the long rod projectile. The striking velocities chosen are 1, 2 and 3 km s^{-1}. The first row describes the plate thickness, ranging from 50 to 200 mm.

The second, third and fourth rows in Table 5 illustrate the effect of an increase in the plate thickness for a given striking velocity on force and momentum time history. The

Table 4. Material properties for target and projectile

Material properties	Target (steel)	Projectile (tungsten)
Dynamic yield strength (GPa)	0.92	1.789
Modulus of elasticity (GPa)	201.5	322.4
Density before impact (kg m^{-3})	7823.0	16981.0
Poisson's ratio	0.295	0.316
Strain hardening value	0.26	—

Table 5. Influence of target thickness and striking velocity on characteristic force–time history

Velocity (km/s)	Target Thickness (mm)		
	50	100	200
1	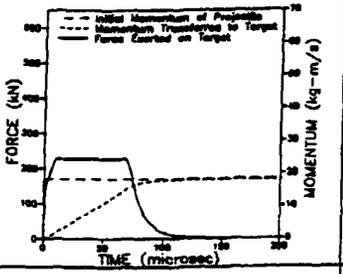	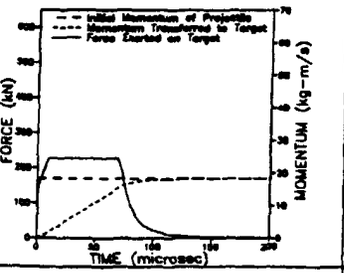	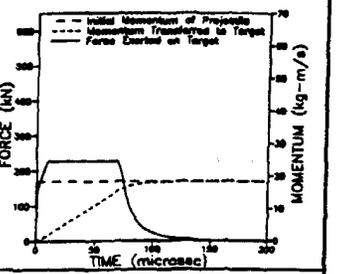
2	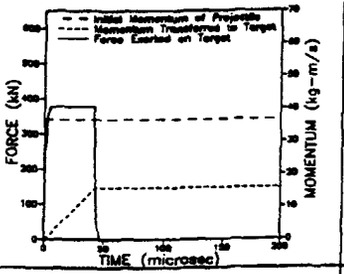	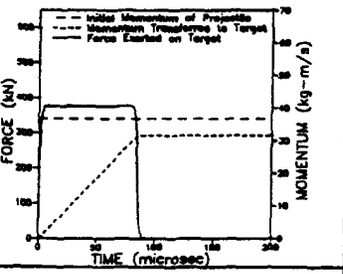	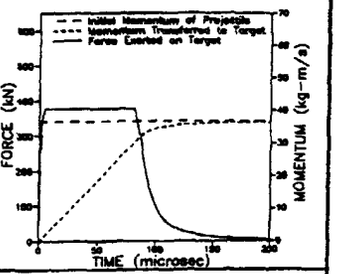
3	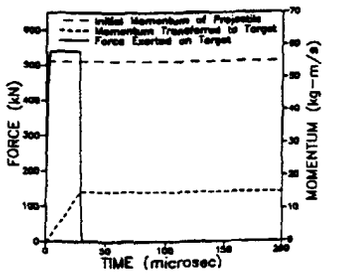	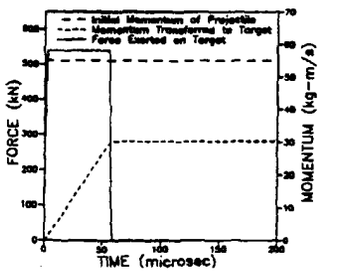	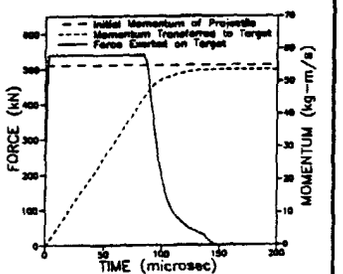

second, third and fourth columns illustrate the effect of increase in the striking velocity of the projectile for a given plate thickness on force and momentum time history.

Initial momentum of the projectile is mass times the striking velocity of the projectile. Increasing the striking velocity of the projectile increases the initial momentum of the projectile. The projectile striking at velocity 1 km s^{-1} to a 50-mm-thick plate, takes 150 μs to transfer all of its initial momentum (18 s^{-1}). This case, where all of the momentum is transferred to the target, represents partial penetration. For a projectile striking at 1 km s^{-1}, the force–time history and the momentum transferred to the target are unaffected by plate thicknesses greater than 50 mm. The maximum peak force remains constant and is not a function of thickness.

By increasing the striking velocity of the projectile from 1 to 2 km s^{-1}, the projectile perforates a 50-mm-thick plate in 48 μs and a 100-mm-thick plate in 96 μs. This indicates that by doubling the plate thickness and maintaining full penetration criteria, the momentum transferred by the projectile penetrating a 50-mm-thick plate is half the momentum transferred by the projectile penetrating a 100-mm-thick plate, and perforation time in a 50 mm plate is half the perforation time in a 100 mm plate. By increasing the plate thickness to 200 mm, the projectile does not perforate, and complete momentum is transferred to the target.

The figures in Table 5 may be compared with Fig. 8. It can be seen that in the case of full penetration $\bar{\beta}$ may be assumed to be constant. In the case of partial penetration eqn (1) in conjunction with eqn (80) must be used. The figures in Table 5 are hypothetical, but illustrate what kinds of force–time histories may be predicted.

Acknowledgement—This work was performed for U. S. Army Research Laboratory, Aberdeen Proving Ground, Maryland, under the contract no. DAAA15-92-K-0001, with Mr Michael Sivack as the program monitor.

REFERENCES

Anderson, C. E. Jr and Walker, J. D. (1991). An examination of long-rod penetration. *Int. J. Impact Engng* **11**, 481–501.

Bishop, R. F., Hill, R. and Mott, N. F. (1945). The theory of indentation and hardness tests. *Proc. Phys. Soc. Lond.* **57**, 147–159.

Forrestal, M. J. and Luk, V. K. (1988). Dynamic spherical cavity expansion in a compressible elastic–plastic solid. *J. Appl. Mech.* **55**, 275–279.

Forrestal, M. J., Luk, V. K. and Brar, N. S. (1990). Perforation of aluminum armor plates with conical-nose projectiles. *Mech. Mater.* **10**, 97–105.

Goodier, J. N. (1945). On the mechanics of indentation and cratering in solid targets of strain-hardening metals by impact of hard and soft spheres. *Proc. 7th Symp. on Hypervelocity Impact*, Vol. III, pp. 215–259. AIAA, New York.

Hanagud, S. and Ross, B. (1971). Large deformation, deep penetration theory for a compressible strain-hardening target material. *AIAA J.* 905–911.

Hopkins, H. G. (1960). Dynamic expansion of spherical cavities in metals. In *Progress in Solid Mechanics* (Edited by R. Hill and I. N. Sneddon), pp. 84–164. Pergamon Press, Oxford.

Johnson, G. R. and Stryk, R. A. (1991). User Instruction for the 1991 Version of the EPIC Research Code. Alliant Tech systems Inc., Air Force Report WL/MN-TR-91-53, October.